



This is a repository copy of *Identification of rotational failure mechanisms in cohesive media using discontinuity layout optimization*.

White Rose Research Online URL for this paper:
<http://eprints.whiterose.ac.uk/78702/>

Version: Published Version

Article:

Smith, C.C. and Gilbert, M. (2013) Identification of rotational failure mechanisms in cohesive media using discontinuity layout optimization. *Geotechnique: International Journal of Soil Mechanics*, 63 (14). 1194 - 1208. ISSN 0016-8505

<https://doi.org/10.1680/geot.12.P.082>

Reuse

Unless indicated otherwise, fulltext items are protected by copyright with all rights reserved. The copyright exception in section 29 of the Copyright, Designs and Patents Act 1988 allows the making of a single copy solely for the purpose of non-commercial research or private study within the limits of fair dealing. The publisher or other rights-holder may allow further reproduction and re-use of this version - refer to the White Rose Research Online record for this item. Where records identify the publisher as the copyright holder, users can verify any specific terms of use on the publisher's website.

Takedown

If you consider content in White Rose Research Online to be in breach of UK law, please notify us by emailing eprints@whiterose.ac.uk including the URL of the record and the reason for the withdrawal request.



eprints@whiterose.ac.uk
<https://eprints.whiterose.ac.uk/>

Identification of rotational failure mechanisms in cohesive media using discontinuity layout optimisation

C. C. SMITH* and M. GILBERT*

Discontinuity layout optimisation (DLO) is a generally applicable numerical limit analysis procedure that can be used to identify critical plastic collapse mechanisms in geotechnical problems. Previous research has focused on using plane-strain DLO to identify mechanisms that are purely translational, or which involve rotations only along predefined boundaries. In this paper a more general formulation, capable of identifying mechanisms that can involve arbitrary rotations and/or translations in cohesive media, is presented. The formulation is then verified through investigation of the yield surface and evolution of the collapse mechanism associated with a footing under combined vertical and moment (V, M) loading, and through study of the well-known anchor uplift problem. It is shown that results of very high accuracy can be obtained, in terms of the collapse load and of the predicted failure mechanism. In the light of the new results, the Bransby design formula for combined vertical and moment loading has been modified to improve its accuracy. Additionally, the more general DLO formulation presented is shown to have several inherent advantages compared with existing numerical limit analysis approaches.

KEYWORDS: limit state design/analysis; plasticity; numerical modelling; bearing capacity

INTRODUCTION

Discontinuity layout optimisation (DLO) is a recently developed numerical limit analysis procedure that can be used to obtain accurate upper-bound solutions for plane-strain collapse problems. It differs from longer-established numerical methods, such as finite-element limit analysis (FELA) (e.g. Lysmer, 1970; Sloan, 1988; Makrodimopoulos & Martin, 2006) and the method of characteristics (Sokolovskii, 1965), in its ability to directly identify critical failure mechanisms in the form of velocity discontinuities for a prescribed numerical discretisation, and to handle singularities in a fully general way. The application of DLO to problems involving purely translational failure mechanisms was described by Smith & Gilbert (2007). Application of the procedure to several geotechnical example problems involving cohesion, friction and self-weight is also described in that work.

Stages in the DLO procedure are illustrated diagrammatically in Figs 1(a)–1(d). The limit analysis problem is couched in terms of (potential) discontinuities interlinking nodes used to discretise the solid region being modelled. Compatibility of displacements associated with discontinuities meeting at a given node is explicitly enforced, while compatibility at locations where discontinuities cross over one another away from a node is implicitly enforced. The critical layout of discontinuities is then identified using rigorous mathematical optimisation techniques (hence the name ‘discontinuity layout optimisation’), with the objective being to find the solution that minimises overall energy dissipation. Such a procedure can identify highly accurate solutions for problems where the critical mechanism is translational. It is important to note that conventional finite or discrete elements are not used at any stage of the solution procedure, marking a significant departure from conventional

element-based methods. This brings several advantages, which will be discussed in the paper.

However, the DLO formulation presented by Smith & Gilbert (2007) identified only mechanisms involving straight-line discontinuities, and hence only translations, to be modelled. This is in contrast to FELA, which can readily model combined translational/rotational mechanisms. An extended formulation allowing rotational mechanisms to be identified using DLO was therefore outlined by Gilbert *et al.* (2010). This involved the use of special boundary discontinuities to allow hybrid rotational/translational mechanisms to be modelled, although it did not permit rotations within a soil mass to be modelled. Although combined translational/rotational mechanisms have been widely considered in the context of metal plasticity (e.g. Chakrabarty, 2009), in the mainstream geotechnical literature they have received sparse attention, although obviously single slip-circle mechanisms are well known. Martin & Randolph (2006) describe one such mechanism suitable for the analysis of lateral pile capacity. A description of the theoretical kinematics of interacting rotating bodies, in a form relevant to the current work, will be provided in the present paper, but from the perspective of DLO the key outcome is that the instantaneous kinematically compatible interface between two rotating bodies in a cohesive (e.g. Tresca) medium takes the form of an arc of a circle, indicating the need for curved as well as straight slip-line discontinuities to be included in a more general DLO formulation.

Thus in this paper a more general DLO formulation is presented that permits identification of mechanisms that can involve completely arbitrary rotations and/or translations in cohesive media, utilising circular arcs in addition to straight-line discontinuities. It is clear from Figs 1(e) and 1(f) that inclusion of these arcs also permits rotational movements to be modelled. (For the sake of clarity, only two circular arcs per node pair are shown in Figs 1(e) and 1(f), but an effectively infinite number of arcs can be considered when using suitable adaptive methods, as will be outlined in the section ‘Modelling rotational mechanisms: adaptive solution scheme’.)

Manuscript received 10 June 2012; revised manuscript accepted 13 May 2013. Published online ahead of print 26 July 2013.

Discussion on this paper closes on 1 April 2014, for further details see p. ii.

* Department of Civil and Structural Engineering, University of Sheffield, UK.

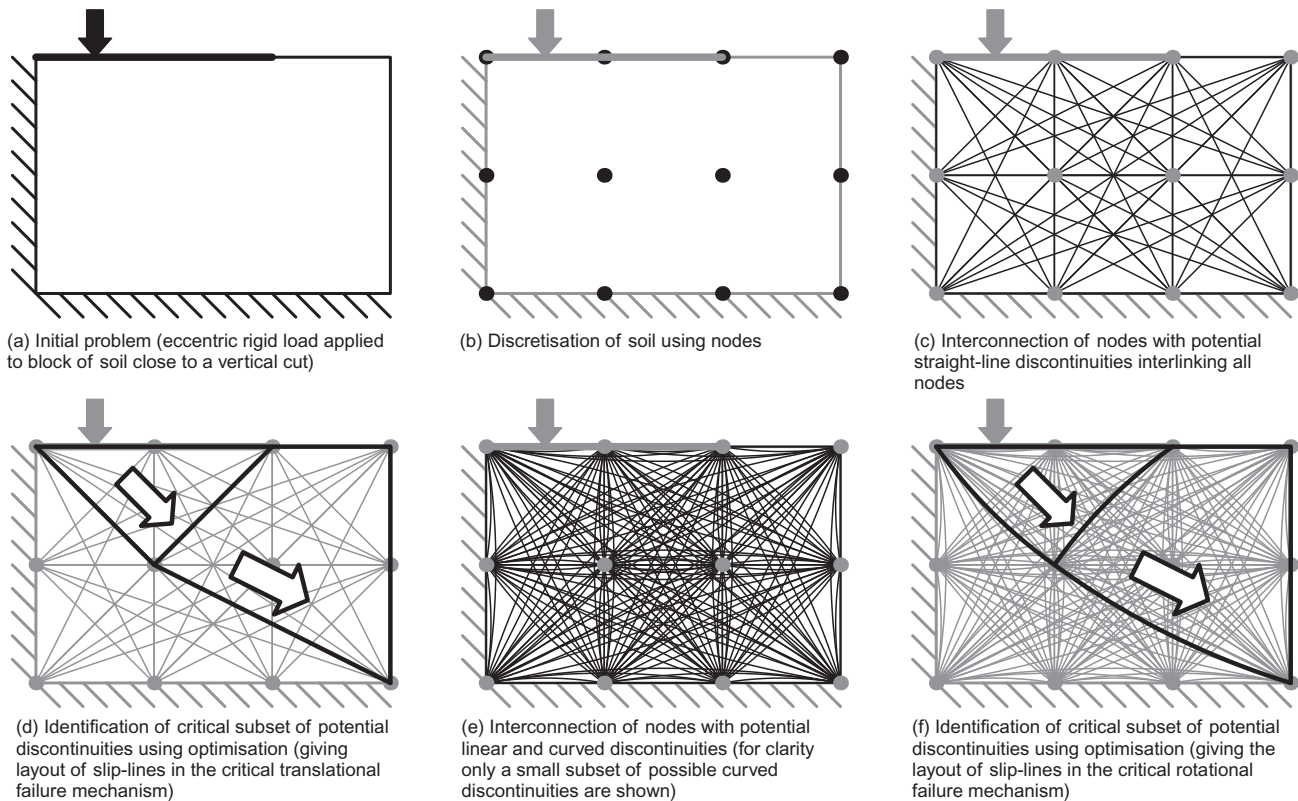


Fig. 1. Stages in the DLO procedure: (a)–(d) translational failure; (a)–(b) and (e)–(f) rotational failure

In this paper the basic DLO formulation, as previously applied to translational problems, will initially be briefly described. Means by which combined rotational/translational compatibility can be handled using the DLO procedure will then be explored, and appropriate energy dissipation terms and a work equation formulated, thus allowing a basic kinematic formulation to be developed. However, to enable larger problems to be tackled, and to allow more refined solutions to be obtained, an adaptive solution procedure will also be described. Finally, the adaptive DLO procedure developed will be used to find the yield surface for a footing under vertical and moment (V , M) loading, allowing the empirical design formula presented by Bransby (2001) to be modified to improve its accuracy, and then also applied to an anchor uplift problem, illustrating the efficacy of the approach.

MODELLING TRANSLATIONAL FAILURE MECHANISMS

Background

As indicated in Figs 1(a)–1(d), in the standard translational DLO formulation a grid of nodes is first distributed across the solid region under consideration, and these nodes are then interconnected with potential straight-line discontinuities. Thus, when a sufficiently fine grid of nodes is employed, the set of potential discontinuities will comprise lines of a wide variety of lengths and orientations. The problem is then to find the critical collapse mechanism, formed from a subset of these potential discontinuities. Therefore with DLO the problem is couched in terms of velocity discontinuities – henceforth for convenience referred to as ‘slip-lines’ – rather than in terms of ‘solid elements’ of fixed geometry. (Here the term ‘slip-line’ simply indicates a line along which sliding occurs. There is no explicit stipulation that the slip-line discontinuities identified must be arranged orthogonally, as would typically be

required when defining a classical ‘slip-line field’; however, the resemblance of a DLO solution to the exact slip-line field solution will be observed to increase as the nodal discretisation is refined.) A key benefit is that the compatibility and work equations for each slip-line discontinuity, which have known orientation and length, are very simple (cf. finite-element-based approaches). In order for the DLO procedure to work, linear superposition must hold for each potential slip-line. Thus the problem must be cast in relative terms. For example, it is necessary to consider the relative displacement jump(s) across the interfaces (or slip-lines) separating the rigid blocks of soil forming the failure mechanism, rather than consider absolute movements of the rigid blocks themselves.

In an upper-bound plasticity problem kinematic compatibility must be preserved, and a solution can be found by minimising the energy dissipated. For a material in which dilation is zero, compatibility can be enforced in DLO by requiring that the vector sum of the relative displacements (or, strictly speaking, displacement rates) s of slip-lines meeting at any node equal zero. Thus, for each node j ($j = 1, 2, \dots, n$) that has n_j slip-lines connected to it

$$\sum_{i=1}^{n_j} \alpha_i s_i = 0 \quad (1)$$

$$\sum_{i=1}^{n_j} \beta_i s_i = 0 \quad (2)$$

where $\alpha_i = \cos \theta_i$ and $\beta_i = \sin \theta_i$ are respectively x -axis and y -axis direction cosines measured from the node, as indicated in Fig. 2, and where s is taken as positive if the body on the right-hand side of the slip-line (viewed from the node) is moving away from the node, relative to the body on the left-hand side.

Furthermore, in a cohesive medium, energy dissipation can be computed by summing the products of the relative

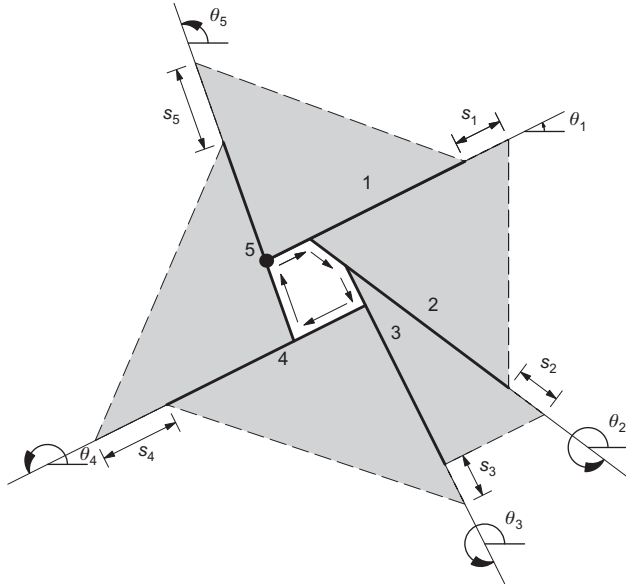


Fig. 2. Instantaneous compatibility of slip-line displacements at a node (translational movements, after Smith & Gilbert, 2007)

slip (s_i), cohesion (c_i) and length (l_i) for each slip-line i . Thus, assuming there are m slip-lines in the problem, the objective function requires minimisation of energy dissipated (E) as follows.

$$\min E = \sum_{i=1}^m c_i l_i |s_i| \quad (3)$$

To avoid the need to consider absolute slip values, it is convenient to replace the $|s_i|$ term in equation (3) with plastic multiplier variables that are explicitly constrained to be non-negative, thereby ensuring energy dissipation is always positive, as outlined in Smith & Gilbert (2007). (The use of plastic multipliers and an associated flow matrix also readily allows other material failure criteria to simultaneously be applied, such as a tensile cut-off. In this case only plastic multiplier variables that describe deformations normal to the active portion of the yield surface will be non-zero.) The general DLO formulation, which incorporates such requirements, and which is amenable to solution using linear programming (LP), is presented in the next section.

General DLO formulation

A plane-strain analysis of a quasi-statically loaded, perfectly plastic cohesive-frictional body discretised using m nodal connections (slip-line discontinuities), n nodes and a single load case can be stated in standard matrix-vector form as follows.

$$\min \lambda \mathbf{f}_L^T \mathbf{d} = -\mathbf{f}_D^T \mathbf{d} + \mathbf{g}^T \mathbf{p} \quad (4a)$$

subject to

$$\mathbf{B} \mathbf{d} = \mathbf{0} \quad (4b)$$

$$\mathbf{N} \mathbf{p} - \mathbf{d} = \mathbf{0} \quad (4c)$$

$$\mathbf{f}_L^T \mathbf{d} = 1 \quad (4d)$$

$$\mathbf{p} \geq \mathbf{0} \quad (4e)$$

where the objective is to minimise energy dissipation (equation (4a)), subject to constraints enforcing energy balance (equation (4a)), nodal compatibility (equation (4b)), plastic flow (equation (4c)) and unit external work by unfactored

live loads (equation (4d)). Equations (1) and (2) are hence represented by equation (4b), and equation (3) becomes the dissipation term in equation (4a). The constraint imposed by equation (4d) is required to avoid obtaining a trivial solution in which all displacement jumps \mathbf{d} (and thus plastic multipliers \mathbf{p}) are zero. The positivity of internal energy dissipation is ensured by inequality (4e).

Considering translational mechanisms only, as considered by Smith & Gilbert (2007), $\mathbf{d}^T = \{s_1, n_1, s_2, n_2, \dots, n_m\}$, where s_i and n_i are the relative shear and normal displacement jumps between blocks at discontinuity i ; $\mathbf{g}^T = \{c_1 l_1, c_1 l_1, c_2 l_2, \dots, c_m l_m\}$, where l_i and c_i are respectively the length and cohesive shear strength of discontinuity i . $\mathbf{f}_D^T = \{f_{D1}^s, f_{D1}^n, f_{D2}^s, f_{D2}^n, \dots, f_{Dm}^s, f_{Dm}^n\}$ and $\mathbf{f}_L^T = \{f_{L1}^s, f_{L1}^n, f_{L2}^s, f_{L2}^n, \dots, f_{Lm}^s, f_{Lm}^n\}$, where f_{Di}^s , f_{Di}^n and f_{Li}^s , f_{Li}^n represent respectively the shear and normal dead and live loads applied locally at discontinuity i ($i = 1 \dots m$). \mathbf{B} is a suitable ($2n \times 2m$) compatibility matrix assembled from equations (1) and (2); \mathbf{N} is a suitable flow matrix, the contents of which depend on the chosen material failure criteria; and \mathbf{p} is a ($2m$) vector of plastic multipliers. In the case of a cohesive material, equation (4c) can be shown in expanded form for one internal slip-line to be

$$\mathbf{N}_i \mathbf{p}_i - \mathbf{d}_i = \begin{bmatrix} 1 & -1 \\ 0 & 0 \end{bmatrix} \begin{bmatrix} p_i^1 \\ p_i^2 \end{bmatrix} - \begin{bmatrix} s_i \\ n_i \end{bmatrix} = \mathbf{0} \quad (5)$$

Hence, for a non-dilating material, the normal displacement jumps n will all be zero for internal slip-lines. However, they may be non-zero at external boundaries. (In the case of external boundaries, the displacements in \mathbf{d} become absolute rather than relative displacements.) Note also that no special treatment is required to model a fixed boundary, and a free boundary can be modelled by locally ensuring that the cohesive shear strength is zero and the plastic flow constraint (equation (4c)) is not applied. The discontinuity displacement jumps in \mathbf{d} and the plastic multipliers in \mathbf{p} are the LP variables.

A simple example illustrating the application of the compatibility and energy dissipation equations to the problem depicted in Fig. 1(d) is presented in Appendix 1.

MODELLING ROTATIONAL MECHANISMS: BASIC FORMULATION

Compatibility

In a general failure mechanism two blocks of material can potentially rotate as well as slide relative to each other along a discontinuity, as shown for example in Fig. 12 in Appendix 2. The inclusion of rotations in addition to translations means that now three separate compatibility equations must be satisfied at nodes. The form of the compatibility equations can be derived by considering a path of infinitesimal radius around each node. If this is traversed round to the same starting point, then there should be no net change in translational or angular displacement.

If the straight-line distance between the end nodes of discontinuity i is l_i , and the relative rotation about the midpoint along this line is ω_i , then equations (1) and (2) must be modified to account for the presence of a normal displacement of magnitude $0.5l_i\omega_i$ at each end of the discontinuity, caused by this rotation.

$$\sum_{i=1}^{n_j} [\alpha_i s_i + \beta_i (0.5l_i \omega_i)] = 0 \quad (6)$$

$$\sum_{i=1}^{n_j} [\beta_i s_i - \alpha_i (0.5l_i \omega_i)] = 0 \quad (7)$$

To ensure no net rotation about a node, an additional constraint is needed that requires that the sum of all relative rotations around a node equals zero.

$$\sum_{i=1}^{n_j} \omega_i = 0 \tag{8}$$

where ω_i is taken as positive if the body on the right-hand side of the slip-line (viewed from the node) is moving anticlockwise relative to the body on the other side of the arc.

However, the form of the discontinuity has not yet been considered; this will be governed by the flow rule, considered in the next section.

Plastic flow (in a cohesive medium)

In a cohesive medium the flow rule typically dictates the presence of curved slip-lines when rotational failures are involved. These curved slip-lines are arcs of a circle, whose curvature is defined by the angle ψ subtended at the arc centre, and which may be determined from the absolute rotations of adjacent rigid bodies, as described in Appendix 2.

For a slip-line i connecting a master node to a slave node, there are four possible combinations of centre of relative rotation, for which it is necessary to define a sign convention. In this paper the convention illustrated in Fig. 3 is utilised, and is defined fully by any two of the three parameters s_i , ω_i and ψ_i . The sign convention for s_i is the same as defined by Smith & Gilbert (2007), and as given above in ‘background’. It is independent of the direction of the straight line linking the nodes. In contrast, the sign convention for ψ_i requires the definition of a master and slave node, such that its half angle measures the clockwise

angle (about the master node) from the straight line linking the nodes to the arc (as illustrated in Fig. 12 of Appendix 2).

The values of ω_i and s_i , and the constant value of ψ_i (for a specific arc), may be related as follows (noting that s_i is the component of velocity jump parallel to the straight line joining the two nodes and measured at the nodes, and that there is no normal displacement jump n along the arc for a purely cohesive material).

$$\omega_i = \frac{2s_i \tan(\psi_i/2)}{l_i} \tag{9}$$

ψ_i is therefore positive if the body on the clockwise side of the arc (about the master node) rotates anticlockwise relative to the body on the anticlockwise side of the arc, as defined above in ‘Compatibility’.

With the discontinuity shape now defined, the type of nodal compatibility enforcement depicted in Fig. 2 is extended to include rotations, as illustrated in Fig. 4.

Energy dissipation

Considering now energy dissipation, the work done in shear along any curved interface is given, as before, by the products of the relative slip across the interface ($r_i w_i$), cohesion (c_i) and arc length ($r_i \psi_i$).

$$E_i = r_i^2 c_i |\omega_i \psi_i| \tag{10}$$

where r_i is the arc radius, and $-\pi < \psi_i < \pi$. Substituting equation (9) in equation (10), taking $l_i = r_i \cos(\psi_i/2)$ and simplifying gives

$$E_i = c_i |s_i| l_i \left(\frac{\psi_i}{\sin \psi_i} \right) \tag{11}$$

where the expression involving ψ_i in parenthesis may readily be pre-computed for each slip-line i . A simple example illustrating the application of the compatibility and energy dissipation equations to the problem depicted in Fig. 1(f) is presented in Appendix 1.

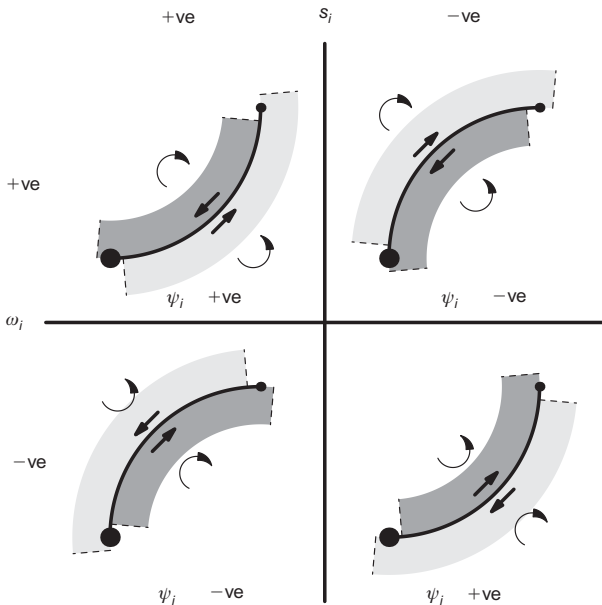


Fig. 3. Combinations of s_i and ω_i . ‘Master’ node is indicated by the larger dot. ψ_i , the angle subtended by the arc at the arc centre, is positive if the arc is located on the clockwise (about master node) side of the chord linking the nodes. s_i is positive if the relative movement vectors (straight arrows) form an anticlockwise ‘couple’. ω_i is positive if the body on the clockwise (about master node) side of the arc is moving anticlockwise relative to the body on the other side of the arc (as indicated by the curved arrows)

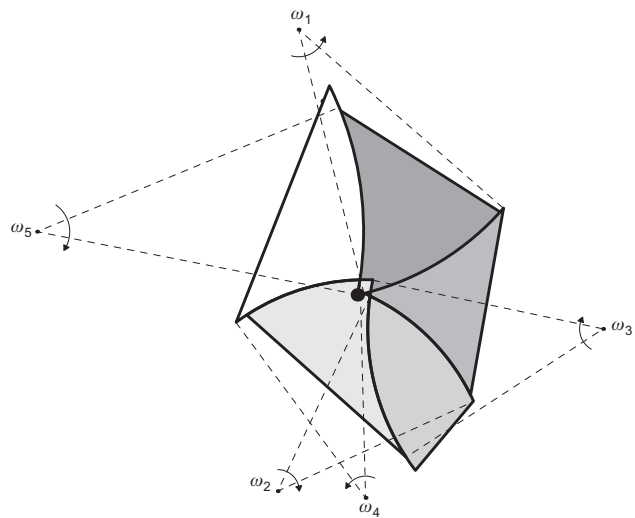


Fig. 4. Instantaneous compatibility of rotational system. Compatibility and flow are enforced at the central node by equations (6), (7) and (9), and overall rotational compatibility by equation (8)

Body forces

Smith & Gilbert (2007) demonstrated that work done by body forces could readily be included in the translational problem formulation. However, the presence of curved slip-lines complicates matters, in that the strip of soil above a discontinuity is now bounded by a curved rather than a straight slip-line. The equations presented for the translational case must thus be extended to include: (a) the increase or decrease in strip area due to the arc; and (b) any work done by rotational movements in addition to translational displacements across the discontinuity. Details of the derivation of the relevant terms are presented in Appendix 3.

Crossover of slip-lines

Crossover of slip-lines is permitted, owing to linear superposition. For example, for any solution or intermediate solution set, suppose that an additional hypothetical node is added at the intersection of a pair of arcs. Each arc is therefore now split into two parts. Each part retains the value of ω of its parent arc, but has a new value of s to reflect its changed chord length, and the change of distance between the centre of rotation and the chord midpoint. Compatibility is ensured, because the relative slips and rotations at the new node will cancel out. Energy dissipation is unchanged, because the relative velocities along the arc boundaries are unchanged. Finally, the work done against body forces is unchanged, because the relative movements across the arc are unchanged.

(However, note that if a new, real node were to be placed at the intersection, and the two original arcs were to be replaced by four new arcs, then the solver might find an improved solution by connecting additional slip-lines to the new node.)

Modified rotational DLO formulation

It is now possible to assemble the derived equations in matrix-vector form. The general formulation given in equation (4) remains valid, but the contents of the various vector and matrix terms need to be modified.

The full rotational compatibility relationship is extended as follows for any node pair AB as

$$\mathbf{B}_i \mathbf{d}_i = \begin{bmatrix} \alpha_i & 0.5l_i\beta_i \\ \beta_i & -0.5l_i\alpha_i \\ 0 & 1 \\ -\alpha_i & 0.5l_i\beta_i \\ -\beta_i & -0.5l_i\alpha_i \\ 0 & -1 \end{bmatrix} \begin{bmatrix} s_i \\ \omega_i \end{bmatrix} \tag{12}$$

where α_i and β_i are respectively x -axis and y -axis direction cosines for slip-line i , connecting nodes A and B in direction A to B, and where s_i is the slip-line displacement, l_i is the straight-line length between nodes, and ω_i is the relative rotation at the discontinuity.

The work equation may be divided into two parts: the self-weight terms, and the dissipation. However, it is preferable to keep terms associated with the curvature of the slip-line together, so the self-weight of the sector between the slip-line and chord connecting any two nodes will be considered together with the dissipation terms. Thus the general self-weight work component (see Appendix 3) may be written as

$$\mathbf{f}_{D,i}^T \mathbf{d}_i = \begin{bmatrix} -W_i\beta_i & -W_i\bar{p}_i \end{bmatrix} \begin{bmatrix} s_i \\ \omega_i \end{bmatrix} \tag{13}$$

where W_i is the total weight of the strip of material lying

vertically above chord i , and \bar{p}_i is the x -coordinate of the centroid of the strip of material relative to the centre of the chord. Live loads are defined similarly.

Calculation of the energy dissipation requires the derivation of plastic multipliers using a flow rule equation (note that ψ_i can be positive or negative).

$$\mathbf{N}_i \mathbf{p}_i - \mathbf{d}_i = \begin{bmatrix} 1 & -1 \\ \frac{2 \tan(\psi_i/2)}{l_i} & -\frac{2 \tan(\psi_i/2)}{l_i} \end{bmatrix} \begin{bmatrix} p_i^1 \\ p_i^2 \end{bmatrix} - \begin{bmatrix} s_i \\ \omega_i \end{bmatrix} = 0 \tag{14}$$

$$\mathbf{p} \geq \mathbf{0} \tag{15}$$

Now the dissipation can be written in terms of s_i or ω_i . Here, to maintain consistency with the translational formulation, it will be written in terms of s_i , although this can change for specific special cases (see later). The energy dissipation is given by

$$\mathbf{g}^T \mathbf{p} \tag{16}$$

where \mathbf{p} takes on the absolute value of \mathbf{s} , and where the dissipation matrix \mathbf{g} , which includes the self-weight of the part of the sector bounded by the slip-line and chord (see Appendix 3), is given by

$$\mathbf{g}^T = \{c_1 C_1 + D_1, c_1 C_1 - D_1, c_2 C_2 + D_2, \dots, c_m C_m - D_m\} \tag{17}$$

where

$$C_i = \frac{\psi_i l_i}{\sin \psi_i} \tag{18}$$

and

$$D_i = \frac{\gamma l_i^2 |\beta_i| \tan(\psi_i/2)}{6} \tag{19}$$

Special cases are as follows: for a straight line, $\psi_i = 0$, $C = l$, $D = 0$. However, for $\psi_i = \pi$ both the flow rule and dissipation equation must be modified as follows.

$$\mathbf{N}_i \mathbf{p}_i - \mathbf{d}_i = \begin{bmatrix} 0 & 0 \\ 1 & -1 \end{bmatrix} \begin{bmatrix} p_i^1 \\ p_i^2 \end{bmatrix} - \begin{bmatrix} s_i \\ \omega_i \end{bmatrix} = 0 \tag{20}$$

$$C_i = \frac{\pi l_i^2}{4} \tag{21}$$

$$D_i = \gamma \frac{l_i^3}{12} |\beta_i| \tag{22}$$

Example problem: maximum height of a vertical cut

This problem has been investigated by a number of researchers, most recently Martin (2011) using FELA to identify the form of a slip-line field (SLF), then solved using the method of characteristics. The SLF solution was used to generate a high-precision solution of $\gamma H/c_u = 3.77649$, where H is the height of the cut. The DLO procedure outlined in the preceding sections was applied to this problem. The volume of soil was discretised using 4, 8, 12, 24 and 48 nodal divisions along the height of the cut, and using a fixed angle ψ of $\pm 10^\circ$ for all discontinuities (i.e. using pairs of potential velocity discontinuities defined by

arcs of fixed curvature for each nodal connection). This gave solutions with corresponding errors of 3.4%, 1.2%, 0.8%, 0.5% and 0.4%, demonstrating that reasonably good results can be obtained even when using low nodal resolutions and a fixed value of ψ . The 48 nodal division solution is shown in Fig. 5.

However, it is evident from Fig. 5 that although the form of the mechanism identified is similar to that proposed by Martin (2011), the funnel-shaped SLF that meets the ground surface is not reproduced well. To obtain an improved solution, more nodal divisions could be employed. Alternatively (or additionally), a greater number of slip-lines of fixed curvature interlinking node pairs could be introduced. However, these options would be likely to increase the computational cost significantly. To address this, an efficient adaptive solution scheme will be described in the next section, and then used to allow much more refined solutions to be obtained for a variety of example problems (see the 'Examples' section).

MODELLING ROTATIONAL MECHANISMS: ADAPTIVE SOLUTION SCHEME

The basic formulation described in the previous section involved pre-specifying a set of slip-line discontinuities of fixed geometry interlinking all nodes. This formulation

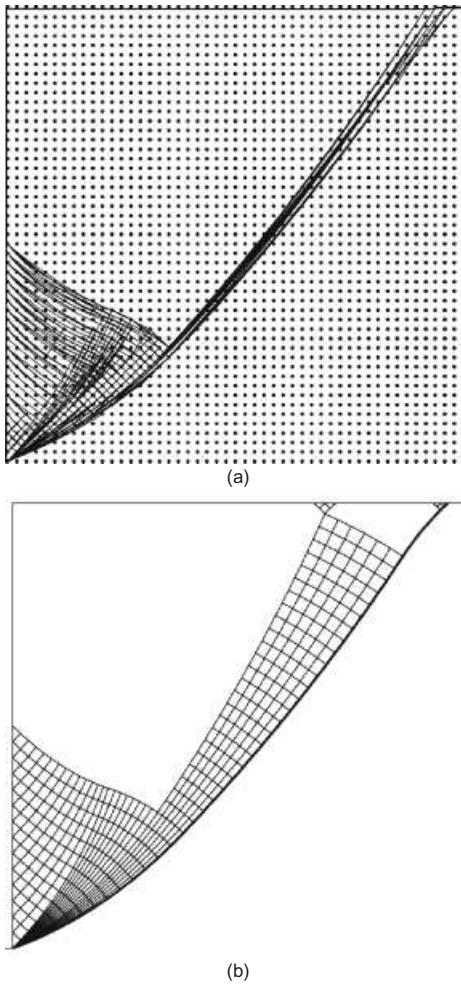


Fig. 5. Slip-line mechanisms for vertical cut problem: (a) DLO solution using basic method with fixed $\psi = \pm 10^\circ$ (48×48 nodal divisions), error 0.4%; (b) Martin (2011) slip-line field solution. Note that slip-lines in the DLO solution are plotted only if the relative slip on the line exceeds a specified tolerance. This can lead to occasional depiction of apparently 'free'-ended slip-lines

allows reasonably accurate solutions to be obtained for many problems. However, to allow significantly more accurate results to be obtained, corresponding to refined problems containing perhaps tens of thousands of nodes and an effectively infinite number of curved slip-line discontinuities interlinking these nodes, a modified solution scheme employing adaptive refinement is required.

At this point it is useful to draw a distinction between discontinuities that are represented in the LP problem, henceforth referred to as *core* discontinuities, and supplementary discontinuities not yet represented in the LP problem, henceforth referred to as *candidate* discontinuities. (Note that, thus far, only *core* discontinuities have been considered.)

The proposed adaptive solution scheme will involve

1. using sparse initial nodal connectivity, involving the connection of only neighbouring nodes with *core* discontinuities of fixed curvature
2. obtaining a solution to the problem, and using the dual equilibrium formulation to enable the forces and moments along *candidate* discontinuities to also be calculated
3. providing an error estimate by identifying the yield violation associated with both *core* discontinuities and *candidate* discontinuities
4. refining the problem to reduce the number of yield violations, achieved by converting *candidate* discontinuities to *core* discontinuities, and refining unrefined *core* discontinuities as necessary
5. iterating from step 1 until a solution requiring no further refinement is found.

The key elements of the scheme will now be considered, starting with the equilibrium formulation.

Equilibrium formulation

In the previous section a kinematic formulation was described, but an equivalent equilibrium formulation can readily be derived using LP duality principles (e.g. Vanderbei, 2007). This formulation involves a dual equilibrium constraint, which can be written for a given discontinuity i as

$$\mathbf{B}_i^T \mathbf{t}_i + \lambda \mathbf{f}_{Li} - \mathbf{q}_i = -\mathbf{f}_{Di} \quad (23)$$

or, in expanded form, as

$$\begin{bmatrix} \alpha_i & \beta_i & 0 & -\alpha_i & -\beta_i & 0 \\ \frac{l_i \beta_i}{2} & -\frac{l_i \alpha_i}{2} & 1 & \frac{l_i \beta_i}{2} & -\frac{l_i \alpha_i}{2} & -1 \end{bmatrix} \begin{bmatrix} t_A^x \\ t_A^y \\ t_A^m \\ t_B^x \\ t_B^y \\ t_B^m \end{bmatrix} + \lambda \begin{bmatrix} f_{Li}^s \\ f_{Li}^m \end{bmatrix} - \begin{bmatrix} S_i \\ M_{Di} \end{bmatrix} = - \begin{bmatrix} f_{Di}^s \\ f_{Di}^m \end{bmatrix} \quad (24)$$

where $\mathbf{t}_i = \{t_A^x, t_A^y, t_A^m, t_B^x, t_B^y, t_B^m\}^T$ contains nodal force variables at nodes A and B (corresponding to the nodal compatibility constraints, and where S_i and M_{Di} represent the shear force and segment weight modified moment acting on the chord i ($i = 1, \dots, m$) respectively. These are also problem variables for core discontinuities in the standard equilibrium

formulation. The required yield constraint can also be written for a candidate discontinuity i as

$$\mathbf{N}_i^T \mathbf{q}_i \leq \mathbf{g}_i \tag{25}$$

or, in expanded form for the Tresca yield condition, as

$$\begin{bmatrix} 1 & \frac{2 \tan(\psi_i/2)}{l_i} \\ -1 & -\frac{2 \tan(\psi_i/2)}{l_i} \end{bmatrix} \begin{bmatrix} S_i \\ M_{Di} \end{bmatrix} \leq \begin{bmatrix} C_i c_i + D_i \\ C_i c_i - D_i \end{bmatrix} \tag{26}$$

Defining

$$\begin{aligned} M &= M_D - \frac{Dl}{2 \tan(\psi/2)} \\ &= M_D - \gamma \frac{l^3}{12} |\beta| \end{aligned} \tag{27}$$

where M is the moment acting on the chord, the yield condition becomes

$$\begin{bmatrix} 1 & \frac{2 \tan(\psi_i/2)}{l_i} \\ -1 & -\frac{2 \tan(\psi_i/2)}{l_i} \end{bmatrix} \begin{bmatrix} S_i \\ M_i \end{bmatrix} \leq \begin{bmatrix} C_i c_i \\ C_i c_i \end{bmatrix} \tag{28}$$

The shear force S and moment M are the forces/moments acting on the chord face of the solid segment delineated by the chord, and arc joining the two nodes under consideration, as shown in Fig. 6. Equation (28) tests whether this combination of S and M would cause yield by slip along the arc specified by ψ .

Error estimation: determining yield violation

Inspection of equation (24) indicates that, once the nodal force variables are known, the shear force \tilde{S} and moment \tilde{M} may be obtained on any chord linking two nodes, where \tilde{S} and \tilde{M} are identical to S and M respectively, except that they are not currently LP variables. Now the yield violation function relates S and M and ψ as follows. Examining the

first constraint in equation (28), the following inequality must hold for yield not to be violated (assuming $0 < \psi < \pi$).

$$S + \frac{2M \tan(\psi/2)}{l} \leq \frac{\psi l c}{\sin \psi} \tag{29}$$

or

$$\left(\frac{S}{lc}\right) \frac{\sin \psi}{\psi} + 4 \left(\frac{M}{l^2 c}\right) \frac{\sin^2(\psi/2)}{\psi} \leq 1 \tag{30}$$

Similarly, the second constraint of equation (28), assuming $0 < \psi < \pi$, gives

$$\left(\frac{S}{lc}\right) \frac{\sin \psi}{\psi} + 4 \left(\frac{M}{l^2 c}\right) \frac{\sin^2(\psi/2)}{\psi} \geq -1 \tag{31}$$

These equations may be used to generate the yield surface depicted in Fig. 7. Note that for the dashed lines (second constraint in equation (28), or equation (31)), positive values of ψ apply to the lower left-hand corner of the graph.

The actual equation of the surface is defined by the value of ψ that gives a minimum value of M for a given S . It can be shown (Appendix 4) that equation (30) is satisfied when

$$\psi = \left(\frac{S}{lc} + 1\right) \tan\left(\frac{\psi}{2}\right) \tag{32}$$

with ψ sharing the same sign as M . Equation (31) is satisfied when

$$\psi = \left(-\frac{S}{lc} + 1\right) \tan\left(\frac{\psi}{2}\right) \tag{33}$$

with ψ taking on the opposite sign to M .

Adaptive algorithm

As already indicated, for large problems it is not generally feasible to interlink all nodes with m_{all} core discontinuities at the outset (with each connection perhaps involving slip-line discontinuities of various curvatures). Instead it is usually much more efficient to begin with minimal initial connectivity comprising m core discontinuities, and to then convert candidate discontinuities to core discontinuities as required, as part of an iterative scheme. In order to identify which of the $\tilde{m} = m_{all} - m$ candidate discontinuities should be added with a view to improving the solution, use can be made of the yield violation calculations described in the preceding section, allowing candidate discontinuities on which yield is violated to be identified.

Thus it is clear from Fig. 7 that any stress point lying outside the yield surface may be considered to violate yield for a range of values of ψ . Adding one or more new linear yield constraints (discontinuities) to the problem, corresponding to these values of ψ , will ensure that in the next iteration this stress point will have to move closer to or within the yield surface. When a solution is obtained in which yield is not violated on any discontinuity (candidate or core), then it is guaranteed that the solution must be equivalent to the one obtained had all the discontinuities been employed in the problem at the outset. This is typically achieved in a small number of iterations.

An example adaptive scheme, similar to that used by Smith & Gilbert (2007) for translational problems, is described in Appendix 5.

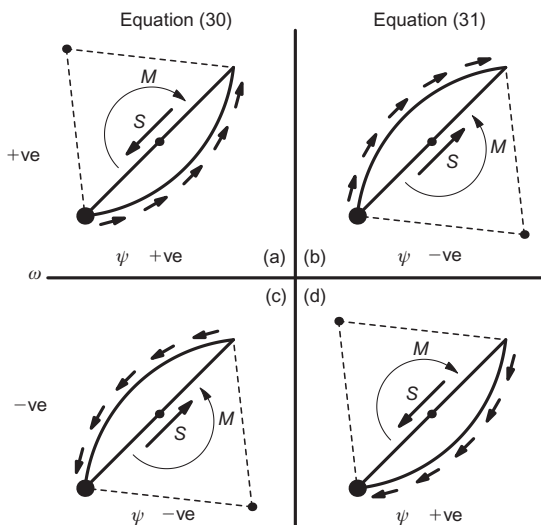


Fig. 6. Interpretation and sign convention for derived dual parameters S and M acting on the chord joining two nodes, for the different scenarios depicted in Fig. 3. The sign of S is independent of the location of the master node. The sign of M is a function of the location of the master node. The small arrows on the circumference of the arc indicate the shear stresses opposing rotation of the segment

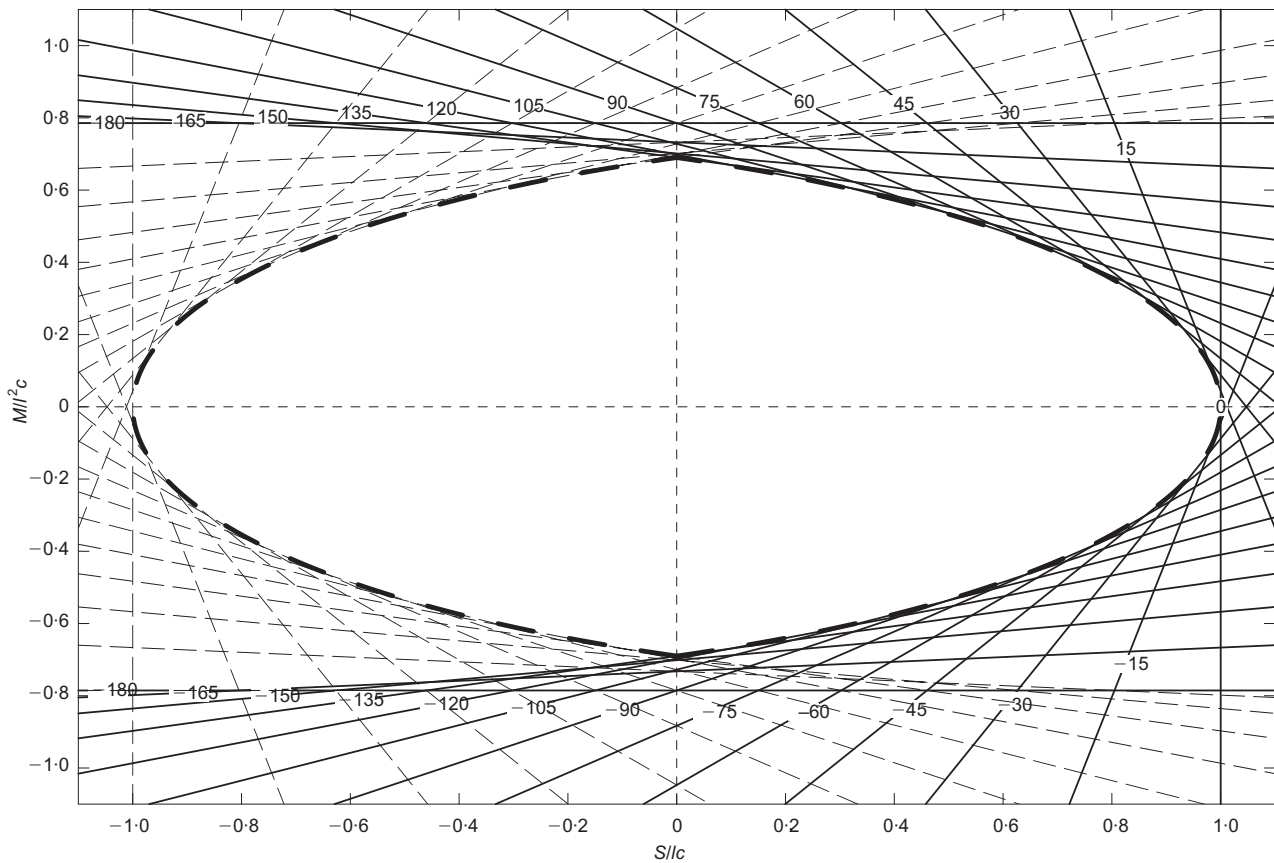


Fig. 7. Yield surface in normalised shear (S)–moment (M) space (thick dashed line). Thin solid lines and dashed lines refer respectively to the first and second constraints in equation (28). Numbers on lines indicate value of ψ in degrees, and are plotted on solid lines only for clarity

EXAMPLES

Footing under combined vertical and moment loading

This problem involves a footing of width B and infinitesimal height located on the surface of a semi-infinite body of soil of undrained strength c , loaded by a vertical load per unit width V and anticlockwise moment per unit width M acting at the footing centreline. For simplicity, it will be assumed here that the soil/footing interface can sustain unlimited tension. The collapse load for $M = 0$ is given by $V_0 = (2 + \pi)cB$ (after Prandtl, 1921), and for $V = 0$ is $M_0 = 0.690025cB^2$.

This problem has been investigated by various researchers, such as Bransby (2001), who proposed the following design formula to determine the bearing capacity for a range of load eccentricities.

$$\frac{M}{M_0} = 1 - \left(\frac{V}{V_0}\right)^4 \tag{34}$$

More recently Martin (2011) presented high-precision values for two specific cases using FELA and the SLF approach.

The DLO procedure employing the iterative adaptive approach outlined in the section ‘Adaptive algorithm’ was applied to this problem. First the $M = 0$ case was considered as a benchmark, using both the original translational formulation (Smith & Gilbert, 2007) and the new procedure presented here; results are listed in Table 1. Using an approach similar to that proposed by Darwich *et al.* (2010), the results were also extrapolated using a power-law fit to provide an estimate of the collapse load that would be computed using an infinite number of nodal divisions (i.e.

Table 1. Values of V/cB^2 derived from DLO analyses for a centrally loaded footing modelled with various nodal divisions utilising either translational or rotational DLO

M/M_0	Exact solution (Prandtl, 1921)	DLO solution method	DLO Resolution (footing nodal divisions)							
			2	5	10	20	50	100	200	∞^*
0.0	$2 + \pi$ (diff: 0.00%)	Translational	5.667 (10.2%)	5.238 (1.88%)	5.190 (0.94%)	5.163 (0.42%)	5.149 (0.14%)	5.144 (0.05%)	5.143 (0.03%)	5.142 (0.01%)
0.0	$2 + \pi$ (diff: 0.00%)	Rotational	5.530 (7.55%)	5.231 (1.74%)	5.173 (0.61%)	5.156 (0.28%)	5.146 (0.09%)	5.143 (0.03%)	5.142 (0.01%)	5.142 [†] (0.00%)

Prandtl (1921) solution of $2 + \pi$ taken as benchmark values for calculating percentage differences shown.

* Extrapolated result, obtained using 50, 60, 70, . . . , 200 nodal divisions.

† Value to six significant figures = 5.14162 (diff: 0.0005%)

the true collapse load). (The only difference from the procedure proposed by Darwich *et al.*, 2010, is that here a weighted rather than normal least-squares regression analysis was performed when conducting the extrapolation, with the weighting factor being taken to be equal to the number of nodal divisions.)

It is clear that, for a given numerical discretisation, the solutions obtained using the present procedure are slightly more accurate than those obtained using the original translational DLO formulation. This is because adjacent blocks of material can if necessary now rotate slightly, relative to each other, helping to overcome limitations associated with a given nodal discretisation. However, the best DLO solution (i.e. 5.142 with 200 nodal divisions) improves on existing FELA upper-bound solutions in the literature (Sloan & Kleeman, 1995; da Silva & Antao, 2007; Makrodimitopoulos & Martin, 2007), and is also better than the approximate rather than strict upper-bound solution recently obtained by Le *et al.* (2010) using a cell-based, smoothed, finite-element procedure. Furthermore, extrapolated solutions are in both cases very close to the exact solution. (When expressed to six significant figures, the extrapolated solution obtained using the present procedure was calculated to be 5.14162, which is in error by just 0.0005%.) This clearly demonstrates the high accuracy of the solutions that can be obtained using the DLO procedure.

The combined vertical load and moment problem was then investigated using values of V/V_0 in increments of 0.125 and a range of nodal resolutions. Selected results are listed in Table 2. Assuming that the present extrapolated results represent the exact solution, it can be seen that highly accurate DLO results, very close to the SLF results of Martin (2011), can again be obtained when using high nodal resolutions. These results also improve on the best available FELA results currently reported in the literature for this problem.

Both the extrapolated results and very low nodal resolution results (using nodal spacings of $B/2$) are also presented in Fig. 8 and compared with other solutions in the literature. It is evident that reasonably good results are obtainable, even for very low nodal resolutions. This demonstrates the ability of the procedure to represent a full range of potential slip-circles, allowing it to handle problems at low resolution that would be extremely challenging for finite-element-based approaches at equivalent resolutions.

It can also be seen that the Bransby (2001) design formula gives conservative results, underestimating capacity by up to $\sim 10\%$. Modifying the exponent used in equation (34) to 4.95 gives a new equation (equation (35)), bringing results to within $\pm 1.1\%$ of the extrapolated values (as shown in Fig. 8).

Table 2. Values of M/cB^2 derived from DLO analyses for eccentrically loaded footings modelled with various nodal divisions

V/V_0	Martin (2011) solutions			DLO							
	Slip-line field	FELA		Resolution (footing nodal divisions)							
		LB	UB	2	5	10	20	50	100	200	∞^\dagger
0.25	0.6900* (diff: 0.00%)	–	–	0.6900 (0.00%)	0.6900 (0.00%)	0.6900 (0.00%)	0.6900 (0.00%)	0.6900 (0.00%)	0.6900 (0.00%)	0.6900 (0.00%)	0.6900 (0.00%)
0.375	– (diff)	–	–	0.6900 (0.38%)	0.6900 (0.38%)	0.6900 (0.38%)	0.6898 (0.35%)	0.6883 (0.13%)	0.6879 (0.07%)	0.6877 (0.04%)	0.6874 (0.00%)
0.5	0.6749 (diff: 0.01%)	0.6689 (–0.89%)	0.6815 (0.98%)	0.6900 (2.25%)	0.6900 (2.25%)	0.6860 (1.66%)	0.6795 (0.70%)	0.6764 (0.24%)	0.6755 (0.10%)	0.6751 (0.04%)	0.6748 (0.00%)
0.625	– (diff)	–	–	0.6900 (9.54%)	0.6720 (6.68%)	0.6524 (3.57%)	0.6419 (1.91%)	0.6340 (0.65%)	0.6316 (0.27%)	0.6306 (0.11%)	0.6299 (0.00%)
0.75	0.5187 (diff: 0.02%)	0.5131 (–1.06%)	0.5216 (0.57%)	0.5885 (13.5%)	0.5731 (10.5%)	0.5483 (5.73%)	0.5322 (2.62%)	0.5231 (0.87%)	0.5204 (0.35%)	0.5194 (0.15%)	0.5186 (0.00%)
0.875	– (diff)	–	–	0.4278 (29.2%)	0.3974 (20.1%)	0.3663 (10.7%)	0.3472 (4.89%)	0.3360 (1.51%)	0.3330 (0.60%)	0.3318 (0.24%)	0.3310 (0.00%)

Extrapolated DLO results taken as benchmark values for calculating percentage differences shown.

* From simple single-rotating-wedge analysis.

† Extrapolated result, obtained using 50, 60, 70, ..., 200 nodal divisions.

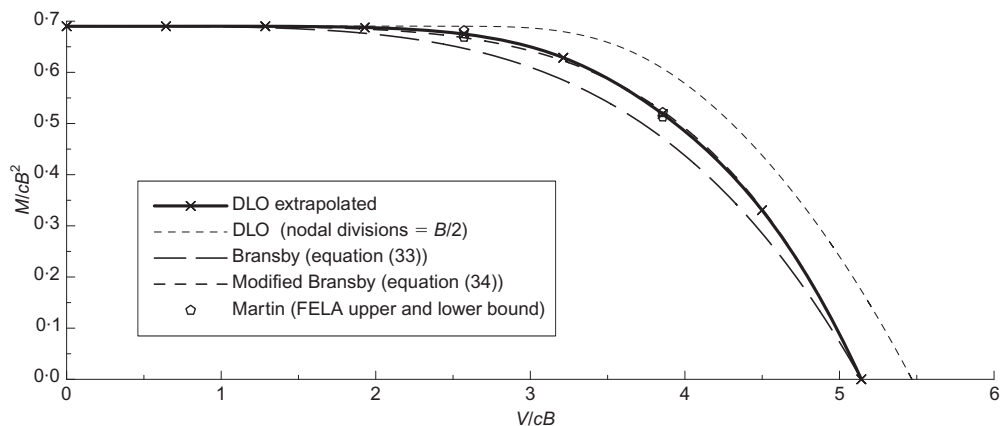


Fig. 8. Normalised V-M yield surface from DLO analysis compared with Bransby (2001) and Martin (2011) results

$$\frac{M}{M_0} = 1 - \left(\frac{V}{V_0}\right)^{4.95} \quad (35)$$

The slip-line solutions for a nodal spacing of $B/100$ and values of V/V_0 of 0.5, 0.75 and 0.95 are shown in Fig. 9, illustrating the evolution of the collapse mechanism as V/V_0 increases. There appear to be five distinct phases: following the formation of a single symmetric arc slip-line for low values of V/V_0 (phase 1), a fan zone forms at the left-hand corner of the footing (Fig. 9(a) – phase 2). This grows to a

certain size, at which point the single slip-line starts to expand into a ‘trumpet’-shaped fan zone (Fig. 9(b) – phase 3). Then, at high values of V/V_0 , the ‘trumpet’ fan zone starts to shrink again, accompanied by growth of a fan zone at the right-hand corner of the footing (Fig. 9(c) – phase 4). Eventually the classic Prandtl mechanism is reached at $V/V_0 = 1.0$ (phase 5).

It can also be seen from these results that the DLO procedure is capable of representing closely the SLF results of Martin (2011). (The reader is also referred to Martin (2011), for examples of the actual kinematics associated

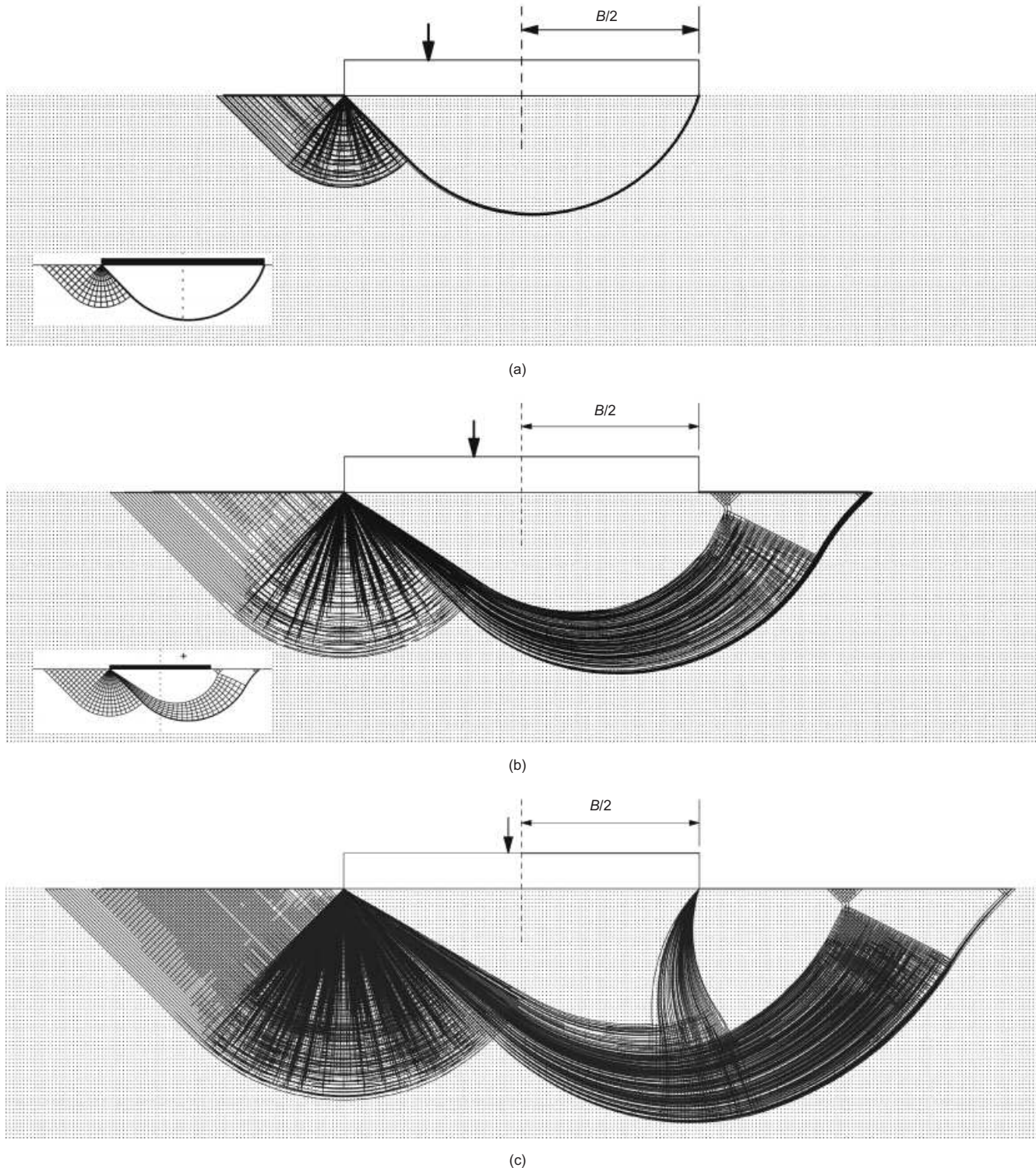


Fig. 9. Evolution of slip-line mechanisms for eccentrically loaded footings as V/V_0 increases, modelled using DLO with nodal spacing equal to footing width/100: (a) $V/V_0 = 0.5$; (b) $V/V_0 = 0.75$; (c) $V/V_0 = 0.95$. Location of applied eccentric load is indicated by arrow. Insets in (a) and (b) show SLF results from Martin (2011) for comparison. The beginnings of a fan zone below the right-hand corner of the footing can be seen in (c), which eventually expands to form a full Prandtl fan zone

with these mechanisms, in the form of deformed meshes.) However, it is important to note that the new solutions described here can be obtained directly, without the need for a two-stage approach of the sort proposed by Martin (the second stage of Martin's approach appears to rely on a solution-specific manual interpretation of the form of the finite-element solution obtained in the first stage). It also: (a) retains the ability to handle singularities in the problem directly; and (b) has the ability to represent a single curved slip-line separating two rigid, non-yielding regions, as clearly illustrated in Fig. 9(a). These are both issues that are challenging for finite-element based approaches.

Anchor uplift

The vertical anchor uplift problem does not have an inherent rotational loading boundary condition, but has a distinctive form of mechanism close to the soil surface that involves rotation. The problem of a horizontal anchor plate of width B , buried at a depth $D = 2B$, was therefore studied using a wide range of nodal spacings from $B/10$ to $B/100$ in steps of 10. The mechanism determined for the $B/100$ nodal spacing problem is presented in Fig. 10, clearly showing the distinctive pattern of velocity discontinuities that form close to the

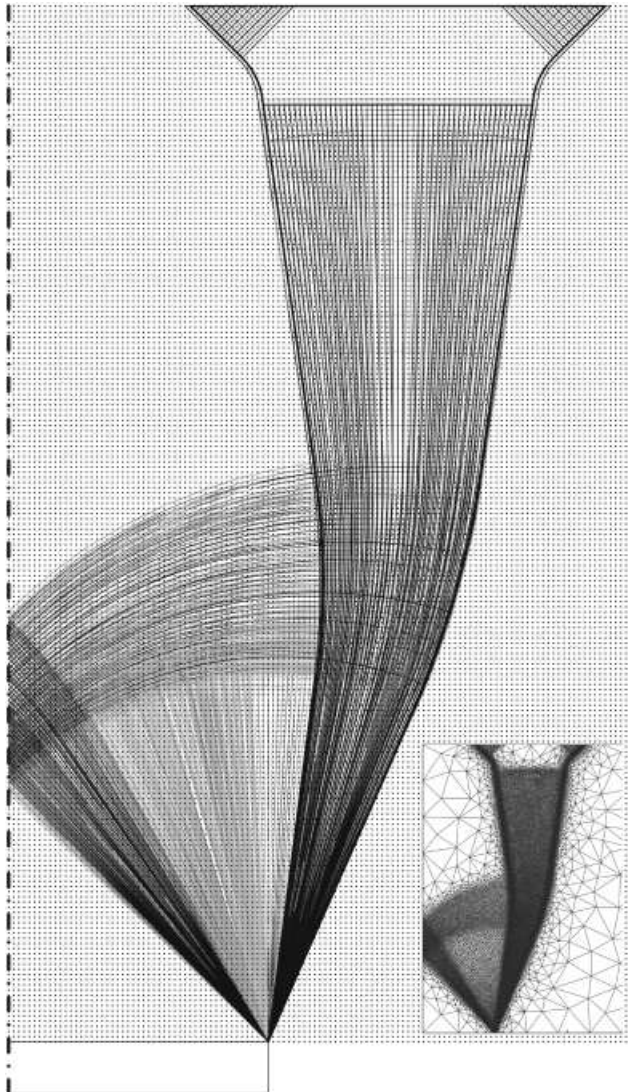


Fig. 10. Half mechanism for vertical uplift of a horizontal anchor plate of width B buried at depth $D = 2.0B$, nodal spacing $B/50$, symmetry line along left-hand edge. Inset shows FELA results from Martin (2009) for comparison

surface, as also observed by Martin (2009). The best upper bound with nodal spacing of $B/100$ was 3.663, which is 0.03% above the extrapolated solution of 3.662 (obtained using the extrapolation scheme described in the previous section based on results from the models with $B/50$, $B/60$, ..., $B/100$). These results compare favourably with those of Martin (2009), who reported FELA lower and upper bounds of 3.654 and 3.668 respectively, giving a mean value of 3.661.

DISCUSSION

The general DLO formulation described herein preserves the essential features of the formulation originally presented by Smith & Gilbert (2007), but allows mechanisms involving curved slip-lines to be identified. By considering the geometry of interacting rotating bodies, it is shown that the additional equations involved are relatively simple (when compared with FELA formulations, for example), and, as can be seen from the example problems presented, singularities are handled inherently and failure mechanisms can readily be visualised.

It is also clear that solutions of very high accuracy can be obtained, with very close approximations of known solutions (normally well within 1%). Solution accuracy appears to be at least as good as that realisable using FELA with mesh adaptivity. It has also been demonstrated that very large problems can be solved using DLO in conjunction with an adaptive solution procedure. In terms of CPU times, considering for example the eccentrically loaded footing with $V/V_0 = 0.5$, solutions within 1% and 0.1% of the analytical solution provided by Martin (2011) were obtained in 2.7 s and 2580 s respectively (total LP solution time when using the Mosek, 2009, solver running on an Intel X5650-powered Linux workstation), indicating that increased accuracy does, however, come at the expense of increased computational cost.

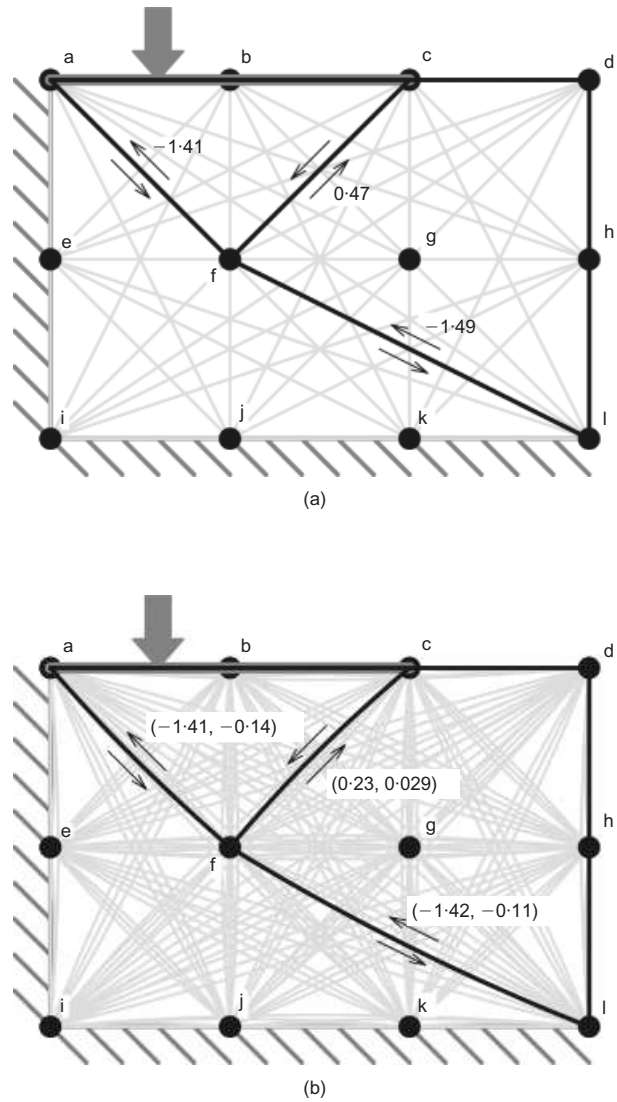
However, one potential disadvantage of the method presented is the need to check that potential curved slip-lines do not extend beyond the problem domain. (When modelling only translational mechanisms with DLO, this is automatically satisfied if the end nodes lie within the problem domain.) This would be an issue if all possible discontinuities had to be checked at the outset. However, use of an adaptive solution scheme means that only a small number of checks actually need to be made. Furthermore, to maintain the upper-bound status of the solution, it is necessary only to check scenarios where a curved slip-line extends into a body with stronger material (or of different unit weight). This means that for problems with simple semi-infinite domains there is no need to make additional checks.

Finally, it may be observed that the basic rotational formulation should in principle be easy to extend to frictional materials, with the derivation of work and self-weight formulae now relating to log spirals rather than circular arcs. However, the additional mathematics are rather more involved than when cohesive media are involved, and detailed consideration of frictional materials is therefore beyond the scope of the present paper.

CONCLUSIONS

(a) The DLO formulation described by Smith & Gilbert (2007) has been extended to handle rotational mechanisms in cohesive media. This has been achieved by using curved slip-lines that take the form of circular arcs. Such an approach allows a rigorous upper-bound solution to be obtained for any undrained plastic limit analysis problem, and retains the inherent ability of the procedure to model singularities, and to provide solutions directly in the form of slip-line mechanisms.

- (b) A basic formulation, in which predefined discontinuities that interlink every node pair in the form of symmetric pairs of arcs of pre-set curvature, has been applied to the well-known vertical cut problem. This allows a reasonable representation of the collapse mode to be obtained, and gives a predicted collapse load that is within 0.5% of the published analytical solution. However, the method rapidly becomes intractably large as the number of nodes increases.
- (c) A refined formulation that involves adaptive addition of slip-line discontinuities of variable curvature has been developed and verified against literature solutions for two classical limit analysis problems in undrained soils: the eccentrically loaded footing, and the anchor uplift problem. Excellent results, ranging from within 0.00% to within 0.25% of the (assumed) exact solutions, have been obtained, together with clear representations of the forms of the critical collapse mechanisms. Furthermore, as the output explicitly shows patterns of slip-line discontinuities, it is arguably more illuminating than the output from FELA.
- (d) For the eccentrically loaded footing problem, five distinct collapse mechanisms were identified. A simple modification to the design equation presented by Bransby (2001) has been suggested, increasing its accuracy to within approximately 1% of the (assumed) exact solutions.
- (e) The ability of the DLO procedure to model a full range of potential slip-circles means that reasonable solutions can often be obtained even when using a very coarse numerical discretisation, particularly when the solution involves only one or two distinct slip-lines (e.g. consider the footing loaded at high eccentricities described herein). Obtaining results of comparable accuracy using most other numerical methods (e.g. finite-element-based methods) would usually necessitate the use of a much finer numerical discretisation, and correspondingly longer run times.



APPENDIX 1: EXAMPLE PROBLEM ILLUSTRATING CALCULATION OF COMPATIBILITY AND ENERGY DISSIPATION

Example solutions for the eccentrically loaded footing problem illustrated in Fig. 1 are presented in Fig. 11(a) for the translational solution mode (equation (4)) and in Fig. 11(b) for the rotational solution mode (equations (12)–(22)). In each problem the (single) vertical live load $f_L = 1$ and the values of d are specified such that $f_L^T d$. The corresponding geometrical and LP parameters used in the energy equations and compatibility equations for node f are given in Table 3. It is clear that for this eccentrically loaded footing problem the rotational solution is more critical than the translational solution.

APPENDIX 2: GEOMETRY OF ROTATING BODIES

Consider two bodies 1 and 2. Let each be rotating, such that the centres of rotation are at (x_1, y_1) and (x_2, y_2) , and let these bodies rotate anticlockwise at angular velocities Ω_1 and Ω_2 respectively, as shown in Fig. 12.

It is straightforward to show that, relative to body 1, body 2 appears to be rotating at an anticlockwise angular velocity $\omega = (\Omega_2 - \Omega_1)$ about an instantaneous centre (x_c, y_c) , where

$$\begin{aligned} x_c &= \frac{x_2 \Omega_2 - x_1 \Omega_1}{\Omega_2 - \Omega_1} \\ &= x_2 + \frac{\Omega_1(x_2 - x_1)}{\Omega_2 - \Omega_1} \\ &= x_1 + \frac{\Omega_2(x_2 - x_1)}{\Omega_2 - \Omega_1} \end{aligned} \quad (36)$$

Fig. 11. Example of compatibility and energy dissipation for simple eccentrically loaded footing problem. (a) Translational solution; values of s are displayed next to arrow pairs. (b) Rotational solution; values of (s, ω) are displayed next to arrow pairs

$$\begin{aligned} y_c &= \frac{y_2 \Omega_2 - y_1 \Omega_1}{\Omega_2 - \Omega_1} \\ &= y_2 + \frac{\Omega_1(y_2 - y_1)}{\Omega_2 - \Omega_1} \\ &= y_1 + \frac{\Omega_2(y_2 - y_1)}{\Omega_2 - \Omega_1} \end{aligned} \quad (37)$$

The shape of the interface between the two bodies depends on the flow rule. For a cohesive material this curve is the arc of a circle; for a frictional material it is a log spiral.

APPENDIX 3: DERIVATION OF BODY FORCE TERMS

Consider the scenario in Fig. 13. Let the body above arc AB be 1 and below be 2. In the first instance it is assumed that body 2 is stationary. Let α and β be direction cosines, as indicated. In this example a positive value of ω indicates clockwise rotation of the body above the arc relative to that below (refer to Fig. 3), taking the master node at A. The work done (E) against gravity for the element above chord AB is given as

$$E = -\bar{x}W\omega \quad (38)$$

where W is the weight of material above chord AB, and \bar{x} is the

Table 3. Energy equations and compatibility equations for node f for eccentrically loaded footing problems depicted in Figs 11(a) and 11(b), founded on weightless cohesive soil with $c = 1$ utilising either translational or rotational DLO

DLO solution method	Discontinuity	Geometry						LP variables			Compatibility at node f [†]		Energy
		θ	l	α	β	ψ	r	d		p			
								s	ω^*	p	$as + 0.5l\beta\omega$	$\beta s - 0.5l\alpha\omega$	
Translational	af	-45.0°	1.41	0.71	-0.71	0.00	∞	-1.41	0.00	1.41	1.00	-1.00	2.00
	cf	-135.0°	1.41	-0.71	-0.71	0.00	∞	0.47	0.00	0.47	0.33	0.33	0.66
	fl	-26.6°	2.24	0.89	-0.45	0.00	∞	-1.49	0.00	1.49	-1.33	0.66	3.33
Sum								0.00	0.00		0.00	0.00	6.00
Rotational	af	-45.0°	1.41	0.71	-0.71	8.04°	10.10	-1.41	-0.14	1.41	1.07	-0.93	2.00
	cf	-135.0°	1.41	-0.71	-0.71	10.00°	8.11	0.23	0.03	0.47	0.15	0.18	0.33
	fl	-26.6°	2.24	0.89	-0.45	10.00°	12.80	-1.42	-0.11	1.49	-1.22	0.75	3.20
Sum								0.00	0.00		0.00	0.00	5.53

Note that $c\psi l p / \sin \psi = clp$ when $\psi = 0$. Discontinuity master node is indicated in bold. For illustrative purposes, the value of ψ was limited to a maximum of 10° in the rotational analysis.

* ω taken as negative in summation if f is the slave node in the discontinuity under consideration.

† $-as + 0.5l\beta\omega$ and $-\beta s - 0.5l\alpha\omega$ are used in the relevant row if f is the slave node in the discontinuity under consideration.

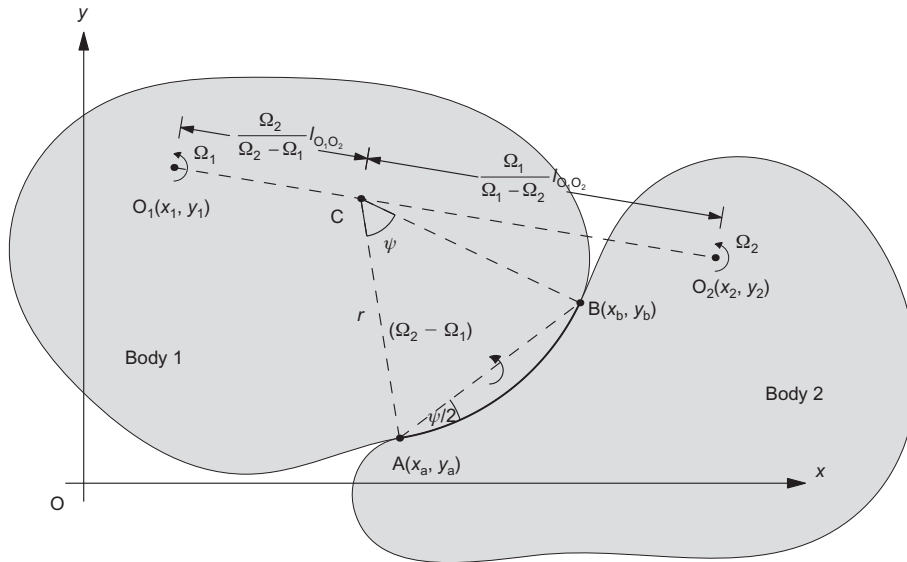


Fig. 12. Examples of compatible interfaces between two bodies 1 and 2, rotating respectively about points O_1 and O_2 with angular velocities Ω_1 and Ω_2 respectively. The relative rotation on the interface AB is $\Omega_2 - \Omega_1$ about point C

horizontal distance (measured in the positive x -direction) from the centroid of the element above AB to its centre of rotation. Hence

$$\begin{aligned}
 E &= -(\beta tl + \bar{p})W\omega \\
 &= -[\beta(tl\omega) + \bar{p}(\omega)]W \\
 &= -[\beta(s) + \bar{p}(\omega)]W
 \end{aligned}
 \tag{39}$$

where \bar{p} is the horizontal distance from C to X in the positive x -direction. For a horizontal surface height h above C, the centroid position \bar{p} is given by

$$\bar{p} = \frac{(\gamma\alpha\beta l^2/2)(-\alpha l/6)}{\gamma\alpha h}
 \tag{40}$$

$$\begin{aligned}
 &= -\frac{\alpha\beta l^2}{12h} \\
 \bar{p}W &= -\frac{\alpha\beta l^2}{12h}\gamma\alpha h \\
 &= -\frac{\gamma\alpha^2\beta l^3}{12}
 \end{aligned}
 \tag{41}$$

It is now necessary to consider the segment of the circle. Taking ψ positive, the centroid of the segment is located a distance \bar{r} on the line from O through C, where

$$\bar{r} = \frac{4r \sin^3(\psi/2)}{3(\psi - \sin \psi)}
 \tag{42}$$

The weight of the segment is given by

$$Q = \gamma \frac{r^2(\psi - \sin \psi)}{2}
 \tag{43}$$

where γ is the unit weight of the material.

The moment M of the sector measured along OC about O is given by

$$\begin{aligned}
 M &= \gamma \frac{2}{3} r^3 \sin^3\left(\frac{\psi}{2}\right) \\
 &= \gamma \frac{l^3}{12}
 \end{aligned}
 \tag{44}$$

Thus additional work done against gravity (for positive ψ) is given by

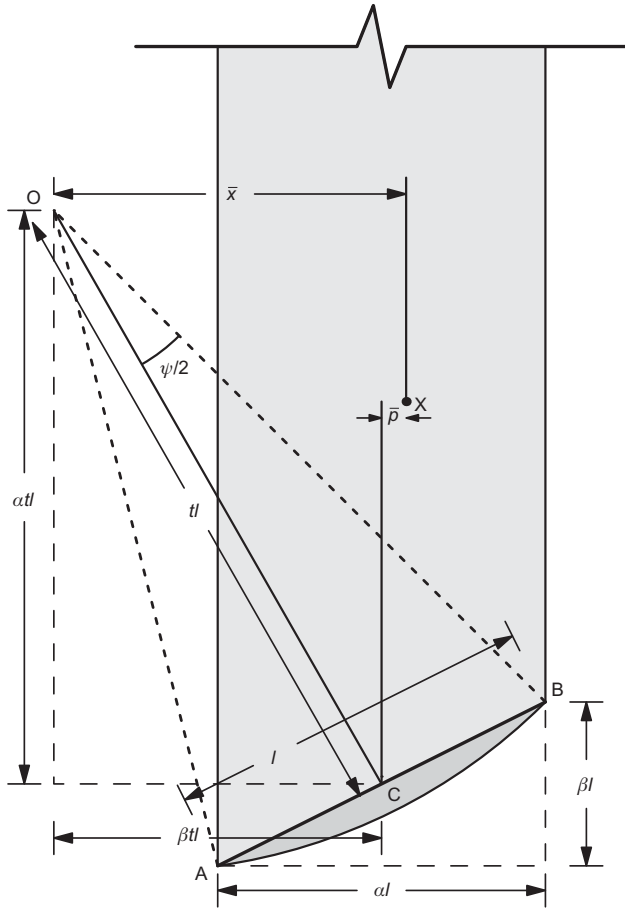


Fig. 13. Treatment of body forces (note that \bar{p} is measured as the horizontal distance from C to X in the positive x -direction)

$$\Delta E = -\gamma \frac{l^3}{12} |\beta| \omega \quad (45)$$

It may be verified that this equation also applies for the four combinations of parameter signs depicted in Fig. 3. Note that this value is constant regardless of ψ ; that is, as ψ increases, the area reduces, but the moment arm increases such that the product stays constant.

Since equation (39) and equation (45) are linear in s and ω , and are defined in relative terms, superposition is permitted.

APPENDIX 4: DERIVATION OF YIELD FUNCTION

In this section the yield function is derived in terms of equation (29) as follows.

$$\tilde{S} \cot\left(\frac{\psi}{2}\right) + \left(\frac{2\tilde{M}}{l}\right) = \frac{\psi lc}{2 \sin^2(\psi/2)} \quad (46)$$

Substituting $x = \cot(\psi/2)$, and differentiating \tilde{M} with respect to x , gives

$$\frac{2 d\tilde{M}}{l dx} = lc [2x \cot^{-1} x - (1+x^2) \sin^2(\cot^{-1} x)] - \tilde{S} \quad (47)$$

Now equate to zero, to find the minimum value of M , and re-substitute x to obtain

$$2 \cot\left(\frac{\psi}{2}\right) \frac{\psi}{2} - \left[1 + \cot^2\left(\frac{\psi}{2}\right)\right] \sin^2\left(\frac{\psi}{2}\right) = \frac{\tilde{S}}{lc} \quad (48)$$

$$\psi = \left(\frac{\tilde{S}}{lc} + 1\right) \tan\left(\frac{\psi}{2}\right) \quad (49)$$

APPENDIX 5: SAMPLE ADAPTIVE SOLUTION ALGORITHM

1. Start by including only core discontinuities that interlink nodes that are near neighbours. (For example, if a rectangular grid with node spacing dx and dy is employed, then only connect nodes with core discontinuities of maximum chord length $\sqrt{dx^2 + dy^2}$.) This connects nodes to nearest neighbours orthogonally and diagonally). For each connection, employ two yield constraints, or slip-lines corresponding to pure translation ($\psi = 0$) and pure rotation ($\psi = \pi$), the latter as defined by equations (20), (21) and (22).
2. Solve problem.
3. For every node pair determine $(|\tilde{S}|/lc, |\tilde{M}|/l^2c)$ using equations (24) and (27).
 - (a) Use equation (32) to determine ψ_a , which represents the point on the yield surface located at the shortest distance from the stress point $(|\tilde{S}|/lc, |\tilde{M}|/l^2c)$ (i.e. along a line normal to the yield surface through the stress point $(|\tilde{S}|/lc, |\tilde{M}|/l^2c)$). Compute proportion of yield violation (based on equation (30))

$$v_a = \left(\frac{|\tilde{S}|}{lc}\right) \frac{\sin \psi_a}{\psi_a} + 4 \left(\frac{|\tilde{M}|}{l^2c}\right) \frac{\sin^2(\psi_a/2)}{\psi_a} \quad (50)$$
 Add constraint (ψ_a, v_a) to list of potential new constraints \tilde{m} .
 - (b) Repeat step 3(a), this time using equation (33) instead of equation (32).
4. Sort the candidate list of new constraints \tilde{m} by magnitude of violation v_a . Add a specified number (e.g. equal to the number of nodes in the problem) from the top of the list to the LP problem. However, exclude any arc that would extend outside the problem domain. If the constraint involves an already connected pair of nodes, then only additional flow rule equations need be added; if not already connected, then both compatibility and flow rule equations need to be added.
5. Repeat from step 2 until no more yield constraints need to be added, to within a specified tolerance.

At this stage the problem is fully solved, and is equivalent to solving the problem where all nodes are connected with all possible arcs from the start.

It is relatively straightforward to check whether an arc extends beyond the problem domain. However, although this would be computationally expensive to check for every potential slip-line, it is a low overhead when only a limited number of candidate slip-lines need to be checked.

NOTATION

c	cohesion
d	displacement
E	energy dissipated
f_D	dead load
f_L	live load
g	work coefficients
l	length of discontinuity
M	moment
m	number of discontinuities
n	number of nodes
p	plastic multiplier
q	discontinuity forces/moments
r	radius of arc
S	shear force
s	relative slip across discontinuity (anticlockwise positive)
t	nodal force variable
V	vertical load
W	weight of soil above specified line
α	$\cos \theta$
β	$\sin \theta$
γ	unit weight
θ	angle of discontinuity measured anticlockwise from horizontal about master node
λ	adequacy factor
ψ	angle subtended at arc centre
Ω	absolute angular velocity
ω	relative rotation

REFERENCES

- Bransby, M. F. (2001). Failure envelopes and plastic potentials for eccentrically loaded surface footings on undrained soil. *Int. J. Numer. Analyt. Methods Geomech.* **25**, No. 4, 329–346.
- Chakrabarty, J. (2009). *Applied plasticity*, 2nd edn. New York, NY, USA: Springer.
- Darwich, W., Gilbert, M. & Tyas, A. (2010). Optimum structure to carry a uniform load between pinned supports. *Struct. Multi-discipl. Optimiz.* **42**, No. 1, 33–42.
- da Silva, M. V. & Antao, A. N. (2007). A non-linear programming method approach for upper bound limit analysis. *Int. J. Numer. Methods Engng* **72**, No. 10, 1192–1218.
- Gilbert, M., Smith, C. & Pritchard, T. (2010). Masonry arch analysis using discontinuity layout optimisation. *Proc. Instn Civ. Engrs – Engng Comput. Mech.* **163**, No. 3, 155–166.
- Le, C., Nguyen-Xuan, H., Askes, H., Bordas, S., Rabczuk, T. & Nguyen-Vinh, H. (2010). A cell-based smoothed finite element method for kinematic limit analysis. *Int. J. Numer. Methods Engng* **83**, No. 12, 1651–1674.
- Lysmer, J. (1970). Limit analysis of plane problems in soil mechanics. *J. Soil Mech. Found. Div. ASCE* **96**, No. 4, 1311–1334.
- Makrodimopoulos, A. & Martin, C. (2006). Lower bound limit analysis of cohesive-frictional materials using second-order cone programming. *Int. J. Numer. Methods Engng* **66**, No. 4, 604–634.
- Makrodimopoulos, A. & Martin, C. M. (2007). Upper bound limit analysis using simplex strain elements and second-order cone programming. *Int. J. Numer. Analyt. Methods Geomech.* **31**, No. 6, 835–865.
- Martin, C. (2009). Undrained collapse of a shallow plane-strain trapdoor. *Géotechnique* **59**, No. 10, 855–863, <http://dx.doi.org/10.1680/geot.8.T.023>.
- Martin, C. (2011). The use of adaptive finite-element limit analysis to reveal slip-line fields. *Géotechnique Lett.* **1**, No. 2, 23–29.
- Martin, C. M. & Randolph, M. F. (2006). Upper-bound analysis of lateral pile capacity in cohesive soil. *Géotechnique* **56**, No. 2, 141–145, <http://dx.doi.org/10.1680/geot.2006.56.2.141>.
- Mosek (2009). *The MOSEK optimization tools manual*, version 6.0. Copenhagen, Denmark: Mosek ApS. See <http://www.mosek.com> (accessed 23/07/2013).
- Prandtl, L. (1921). Hauptaufsätze: Über die eindringungsfestigkeit (härte) plastischer baustoffe und die festigkeit von schneiden. *Z. Angew. Math. Mech.* **1**, No. 1, 15–20 (in German).
- Sloan, S. W. (1988). Lower bound limit analysis using finite elements and linear programming. *Int. J. Numer. Analyt. Methods Geomech.* **12**, No. 1, 61–77.
- Sloan, S. W. & Kleeman, P. W. (1995). Upper bound limit analysis using discontinuous velocity fields. *Comput. Methods Appl. Mech. Engng* **127**, No. 1, 293–314.
- Smith, C. & Gilbert, M. (2007). Application of discontinuity layout optimization to plane plasticity problems. *Proc. R. Soc. A* **463**, No. 2086, 2461–2484.
- Sokolovskii, V. (1965). *Statics of granular media*. Oxford, UK: Pergamon Press.
- Vanderbei, R. J. (2007). *Linear programming: Foundations and extensions*, 3rd edn. London, UK: Kluwer Academic.